JM PAPERS

Perfect active absorption of water waves in a channel by a dipole source

Léo-Paul Euvé[1],†, Kim Pham[2], Philippe Petitjeans[1], Vincent Pagneux[3] and Agnès Maurel[4]

[1]Lab. de Physique et Mécanique des Milieux Hétérogènes (PMMH), ESPCI-PSL, CNRS, Sorbonne University, Univ. Paris Cité, 7 quai Saint Bernard, 75005 Paris, France

[2]LMI, ENSTA Paris, Institut Polytechnique de Paris, 91120 Palaiseau, France

[3]Laboratoire d'Acoustique de l'Université du Mans (LAUM), UMR 6613, Institut d'Acoustique – Graduate School (IA-GS), CNRS, 72085 Le Mans Université, France

[4]Institut Langevin, ESPCI Paris, PSL University, CNRS, 1 rue Jussieu, 75005 Paris, France

This study investigates the potential use of an active device to efficiently absorb water waves propagating in a channel. The active device comprises a dipole source consisting of two sources in quasi-opposition of phase. We explore the feasibility of this approach to achieve perfect absorption of guided waves through interference phenomena. To accomplish this, we establish the law governing the waves emitted by the dipole source to optimize the absorption of specific incident waves. The validity of this law is demonstrated through numerical simulations and laboratory experiments, encompassing both the harmonic and transient regimes of the experimental set-up.

Key words: surface gravity waves, wave scattering

1. Introduction

The efficient absorption of water waves energy is of prime importance in mitigating their deleterious effects on coastal zones. Addressing and minimizing these impacts pose significant challenges in preserving exposed communities, ecosystems and infrastructure. In pursuit of this objective, passive systems have been proposed, falling into two sub-categories. On the one hand, we find large structures such as artificial reefs, typically constructed using concrete, rock or recycled tires (Sollitt & Cross 1972; van der Meer *et al.* 2005; van den Brekel 2021; van Gent *et al.* 2023) or using porous type media, including coastal vegetation, sand dunes or sedimentary layers (Zhu 2001; Silva, Salles & Palacio 2002; Barman & Bora 2021). While these structures can efficiently absorb wave energy,

† Email address for correspondence: leo-paul.euve@espci.fr

they come at the cost of significant dimensions, of the order of several wavelengths. On the other hand, there are technologies designed for capturing and converting wave energy that may be small in size relative to the wavelength (Salter 1974; Guo & Ringwood 2021; Jin & Greaves 2021). However, they absorb only a small portion of the wave energy, as their primary purpose is energy harvesting rather than the creation of a protected zone.

In contrast to passive absorbers, devices based on active absorption aim to completely cancel outgoing waves from the device. In their classic form, developed over the last sixty years, active absorbers operate by reflection only. They are commonly referred to as 'absorbing wavemakers' or 'reflection compensation systems' and are employed to generate waves while avoiding undesired reflections, and minimizing disturbances related to artificial boundaries in wave testing facilities. The perfect absorption obtained is made possible by a destructive interference mechanism between the incident wave, whose reflection is to be cancelled, and the wave generated by the active source, i.e. the moving wall hit by the incident wave (Milgram 1965, 1970; Schäffer & Klopman 2000).

In this study, we demonstrate theoretically, numerically and experimentally that a dipole source device can be employed to achieve perfect active absorption of an incident wave in a channel, simultaneously cancelling its reflection and transmission; see figure 1. This device is inspired by the one investigated in Euvé *et al.* (2023), where perfect passive absorption was achieved using two closely spaced, phase-shifted resonators, whose geometry was carefully tuned for viscous losses and resonance frequency. Here, by actively replicating the absorption conditions observed in that system, we achieve perfect absorption adaptable to any low-frequency incident wave and any loss level. To illustrate the principle of active absorption and its effectiveness, the sections of this paper are structured as follows. The theoretical formulation and numerical validation of the device principle are presented in § 2. The experimental implementation is detailed in § 3, along with an examination of the fields generated solely by the dipole source and the resulting efficient absorption in the harmonic and transient regimes. Brief conclusions are eventually drawn in § 4.

2. Perfect absorption: modelling and numerical validation

We consider the propagation of water waves within a channel characterized by width d and water depth h. The channel contains two extended sources positioned along one of its vertical walls, forming a dipole source that induces inflows/outflows into the channel. The two sources, rectangular and identical, have horizontal and vertical dimensions (a, b), with their centres submerged at depth h_o and spaced along the x-axis at a distance e. Our modelling approach begins with the full three-dimensional (3-D) problem set in $\Omega = \{x \in (-\infty, +\infty), y \in (0, d), z \in (-h, 0)\}$, with the origin at the mean free surface, and z directed vertically upwards. Assuming an inviscid, incompressible fluid and irrotational motion, the velocity potential $\phi(\boldsymbol{r}, t)$ and associated velocity $\boldsymbol{u}(\boldsymbol{r}, t)$ satisfy

$$\text{3-D problem} \quad \begin{cases} \boldsymbol{u} = \boldsymbol{\nabla}\phi, \quad \boldsymbol{\nabla} \cdot \boldsymbol{u} = 0, \quad \text{in } \Omega, \\ u_{z|z=0} = -\dfrac{1}{g}\dfrac{\partial^2 \phi}{\partial t^2}\Big|_{z=0}, \quad u_{z|z=-h} = 0, \\ u_{y|\Gamma} = 0, \quad u_{y|\Gamma_i} = U_i, \quad i = 1, 2, \end{cases} \tag{2.1}$$
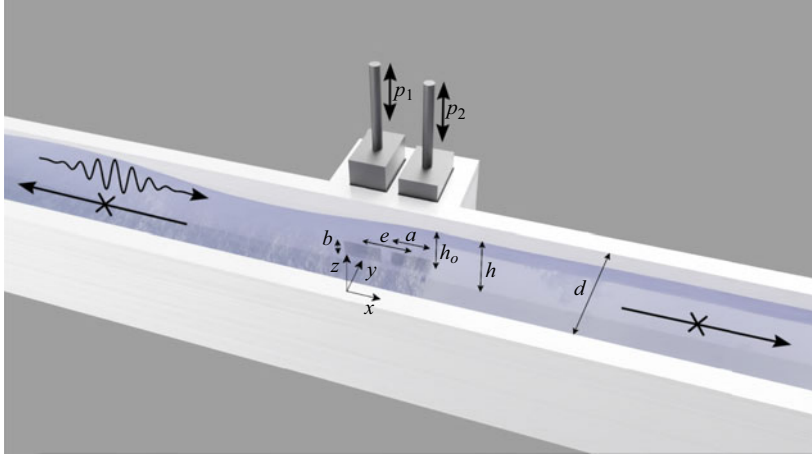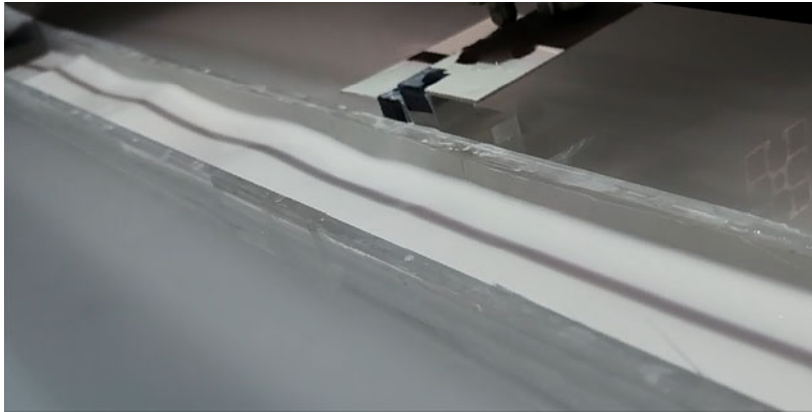
Figure 1. Perfect absorption by a dipole source. (*a*) Schematic view of the experimental set-up. (*b*) Experimental realization of the dipole source producing asymmetric wave propagation in the guide. The waves are visualized by a black line projected onto the free surface of the water, made diffusive by a white dye.

where g is the gravitational constant, t is time, and $\boldsymbol{r} = (x, y, z)$. We have defined the surfaces Γ_i, $i = 1, 2$, and Γ as

$$
\left.
\begin{aligned}
\Gamma_1 &= \{(x + e/2) \in (-a/2, a/2), y = d, (z - h_o) \in (-b/2, b/2)\}, \\
\Gamma_2 &= \{(x - e/2) \in (-a/2, a/2), y = d, (z - h_o) \in (-b/2, b/2)\}, \\
\Gamma &= \{x \in (-\infty, \infty), y \in \{0, d\}, z \in (-h, 0)\} \setminus (\Gamma_1 \cup \Gamma_2),
\end{aligned}
\right\}
\tag{2.2}
$$

which correspond respectively to the regions of the vertical walls occupied by the two sources and the rigid regions of the vertical walls.

2.1. *Reduction of the model: the two-dimensional problem*

In the harmonic regime with time dependence $e^{-i\omega t}$, we go from the 3-D problem to a two-dimensional (2-D) reduced problem. To achieve this, we employ the modal

representation of the 3-D solution

$$\phi(\boldsymbol{r}, t) = e^{-i\omega t} \sum_{n \geq 0} \varphi_n(x, y) f_n(z), \tag{2.3}$$

where

$$f_n(z) = \frac{\cosh k_n(z + h)}{\cosh k_n h}, \quad k_n \tanh k_n h = \frac{\omega^2}{g}, \tag{2.4a,b}$$

such that

$$\int_{-h}^{0} f_m(z) f_n(z) \, dz = N_n \delta_{mn}, \quad N_n = \frac{\sinh(2k_n h) + 2k_n h}{4k_n \cosh^2(k_n h)}. \tag{2.5a,b}$$

Rearranging (2.3) into (2.1) and projecting onto $f_0(z)$ results in a 2-D problem satisfied by $\varphi(x, y) = \varphi_0(x, y)$ in $\Sigma = \{x \in (-\infty, +\infty), y \in (0, d)\}$ (and we also note $k = k_0$ as the real-valued wavenumber of the propagating water waves) of the form

$$\text{2-D problem} \quad \begin{cases} \Delta\varphi + k^2\varphi = 0, & \text{in } \Sigma, \\ \dfrac{\partial\varphi}{\partial y}_{|\gamma} = 0, & \dfrac{\partial\varphi}{\partial y}_{|\gamma_i} = u_i, \quad i = 1, 2, \end{cases} \tag{2.6}$$

where

$$\gamma_1 = \{(x + e/2) \in (-a/2, a/2), y = d\}, \quad \gamma_2 = \{(x - e/2) \in (-a/2, a/2), y = d\}, \\ \gamma = \{x \in (-\infty, \infty), y \in \{0, d\}\} \setminus (\gamma_1 \cup \gamma_2), \tag{2.7}$$

and

$$u_i = \alpha U_i, \quad \alpha = \frac{8 \cosh(kh) \cosh(k(h - h_o)) \sinh(kb/2)}{\sinh(2kh) + 2kh}. \tag{2.8a,b}$$

We consider an incident wave propagating to the right, characterized by a complex amplitude φ_{inc} and sufficiently low frequency such that $kd < 2\pi$, implying that only one mode, independent of y, is propagating in the 2-D guide. Accordingly, the solution of (2.6) away from the dipole source takes the form

$$\varphi(x, y) \simeq \varphi_{inc} e^{ikx} + \varphi^- e^{-ikx}, \quad x \to -\infty, \\ \varphi(x, y) \simeq \varphi^+ e^{ikx}, \quad x \to +\infty, \tag{2.9}$$

where φ^- and φ^+ represent the complex amplitudes of left and right outgoing waves, respectively. The 2-D problem (2.6) can be solved explicitly. In particular, simple expressions for (φ^-, φ^+) in (2.9) are obtained through Green's identity, as elaborated in Appendix A. They read

$$\varphi^- = \frac{i \sin(ka/2)}{k^2 d} \left(u_1 e^{-ike/2} + u_2 e^{ike/2} \right), \\ \varphi^+ = \varphi_{inc} + \varphi_0^+, \quad \varphi_0^+ = \frac{i \sin(ka/2)}{k^2 d} \left(u_1 e^{ike/2} + u_2 e^{-ike/2} \right). \tag{2.10}$$

We will now establish the conditions on (u_1, u_2) necessary to achieve perfect absorption of the incident wave, i.e. to ensure that $\varphi^- = \varphi^+ = 0$. We can already note a specific scenario when $ka = 2n\pi$, where n is an integer, and $kd < \pi$. In this case, $\varphi^- = \varphi_0^+ = 0$
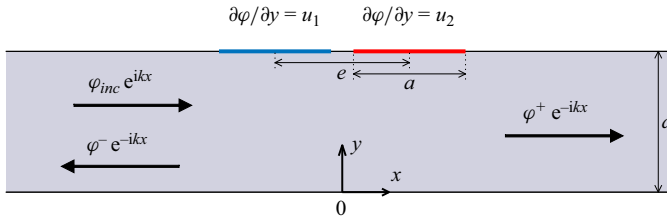
Figure 2. The two-dimensional reduced problem with extended sources considered in the numerics.

regardless of the value of φ_{inc} and the values of u_1 and u_2. These solutions satisfy $\varphi \to 0$ as $x \to \pm\infty$ with $\partial_y\varphi$ remaining constant along γ_i, where $i = 1$ or 2, and they are associated with the superposition of two localized eigenmodes; see Appendix B. Note that this particular scenario renders the sources inactive regarding the incident wave, with $\varphi^- = 0$ and $\varphi^+ = \varphi_{inc}$ whatever the values of (u_1, u_2). Then for $ka \neq 2n\pi$, $\varphi^- = 0$ is obtained from (2.10) if (u_1, u_2) satisfy the relation

$$u_2 = -u_1\, e^{-ike}, \tag{2.11}$$

which remains valid regardless of the presence or absence of an incoming wave in the guide. Subsequently, in the presence of an incoming wave and when the above condition is met, $\varphi^+ = 0$ is possible if condition

$$u_1 = \frac{k^2 d}{2\sin(ka/2)\sin(ke)}\, e^{ike/2}\, \varphi_{inc} \tag{2.12}$$

is also satisfied. Once again, we notice a specific scenario when $ke = n\pi$, where n is an integer. In these cases, the solutions satisfy $\varphi \to 0$ as $x \to \pm\infty$ and either (i) $\partial_y\varphi = C$ along γ_1, and $\partial_y\varphi = -C$ along γ_2, or (ii) $\partial_y\varphi = C$ along γ_1 and γ_2, where C is a constant. Similar to the previous scenario, these solutions are associated with localized eigenmodes (see Appendix B) and inactive sources with $\varphi^- = 0$ and $\varphi^+ = \varphi_{inc}$.

2.2. *Numerical validation of the model*

In this subsection, we inspect the validity of the model by comparisons with direct numerics. The numerical computations are performed using the PDE tool in Matlab, which employs the finite element method to solve partial differential equations. We consider the geometry depicted in figure 2, and apply radiation conditions at the ends of the guide $x = \pm x_M$, consistent with (2.9) for $x_M \gg (a + e)/2$. Specifically, we impose $\partial_x\varphi + ik\varphi = 2ik\varphi_{inc}\, e^{ikx_M}$ at $x = -x_M$, and $\partial_x\varphi - ik\varphi = 0$ at $x = x_M$, consistent with (2.9).

To begin with, we consider the amplitudes (φ^-, φ_0^+) generated solely by the sources; in the model, they are determined by (2.10) with $\varphi_{inc} = 0$. Figure 3 shows the variations of these quantities, normalized to (au_1), against the phase and amplitude of (u_2/u_1), from direct numerics (figures 3a,b) and from the model, (2.10) (figures 3c,d). The agreement between the two sets of results is excellent, showing a relative discrepancy of only 0.1 % (we have considered $kd = \pi/2$, $ka = \pi/4$ and $ke = \pi/4$). Numerically, this representation for $\varphi_{inc} = 0$ is sufficient to determine the couple (u_1, u_2) capable of achieving perfect absorption $\varphi^- = \varphi^+ = 0$. We begin by determining $\xi = u_2/u_1$ that yields $\varphi^- = 0$, since this condition is independent of the value of φ_{inc}. In figure 3, $\varphi^- = 0$ is obtained for $\xi = e^{2.36i}$ (white cross), aligning well with (2.11). We then determine the value of
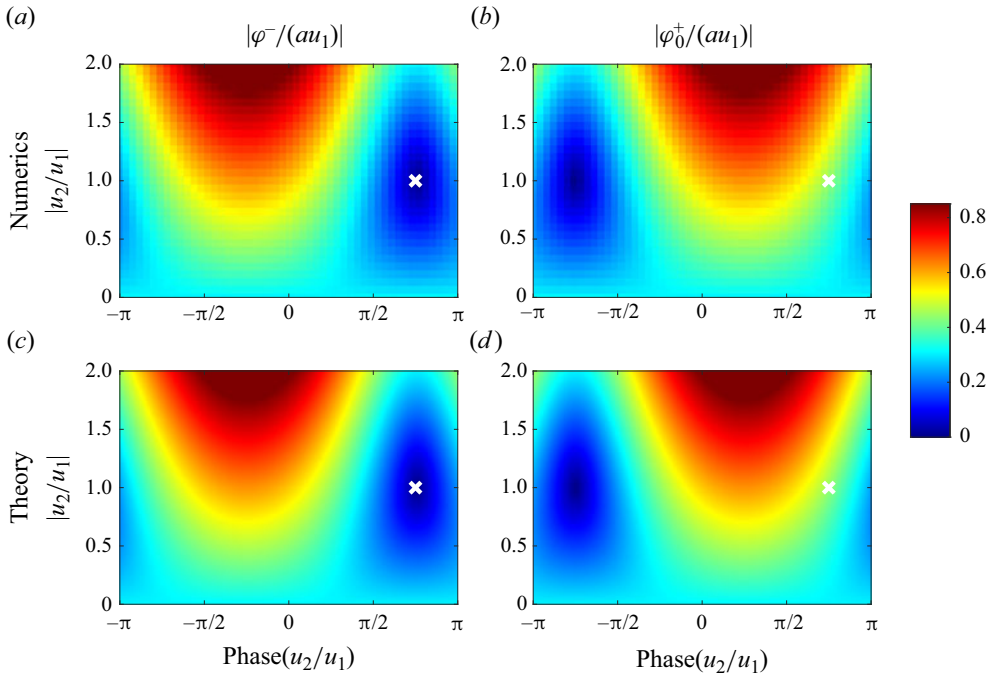
Figure 3. Validation of the model – wave amplitudes of the outgoing waves (φ^-, φ^+) normalized to (au_1) as a function of the source amplitude ratio u_2/u_1 (modulus and phase) obtained numerically and theoretically for $\varphi_{inc} = 0$. The white crosses indicate the theoretical prediction for $\varphi^- = 0$ from (2.11). The parameters are $kd = \pi/2$, $ka = \pi/4$ and $ke = \pi/4$.

$\chi = -\varphi_0^+/(au_1)$ for $u_2/u_1 = \xi$. Eventually, in the presence of any incident wave φ_{inc}, the condition $\varphi^+ = 0$ is obtained simply by linearity when $\varphi_{inc}/(au_1) = \chi$. In the case reported in figure 3, we obtain $\chi \simeq 0.44\,\mathrm{e}^{-0.4\mathrm{i}}$, demonstrating again good agreement with the model; see (2.12). We notice that in practice, for any incident wave φ_{inc}, perfect absorption is achieved by imposing

$$u_1 = \frac{\varphi_{inc}}{a\chi}, \quad u_2 = \xi u_1. \tag{2.13a,b}$$

The above relations involve (ξ, χ), which depend on the frequency and on the geometry of the guide through (ka, ke, kd). Numerically, they are determined from the analysis of representations as those of figure 3; theoretically, they are given by

$$\xi = -\mathrm{e}^{-\mathrm{i}ke}, \quad \chi = \frac{2\sin(ka/2)\sin(ke)}{k^2ad}\,\mathrm{e}^{-\mathrm{i}ke/2}. \tag{2.14a,b}$$

Results in figure 4 showcase variations of (ξ, χ) determined numerically as a function the non-dimensional distance between the two sources $ke \in (0, 2\pi)$ (with $kd = \pi/2$ and $ka = \pi/4$), the source extension $ka \in (0, 2.5\pi)$ (with $kd = \pi/2$ and $ke = 2.5\pi$), and the channel width $kd \in (0, \pi)$ (with $ka = \pi/4$ and $ke = \pi/4$). The theoretical predictions (2.13a,b) are represented by solid lines for comparison, showing excellent agreement over large ranges of the parameters. It is noteworthy that for small ke, implying small ka (figure 4a), the two sources producing perfect absorption are nearly in phase opposition, hence they indeed behave as a dipole source. We also encounter the specific scenarios of inactive sources $\varphi^- = \varphi_0^+ = 0$, hence $\varphi_{inc} = 0$, for $ke = \pi$ or for $ka = 2\pi$.
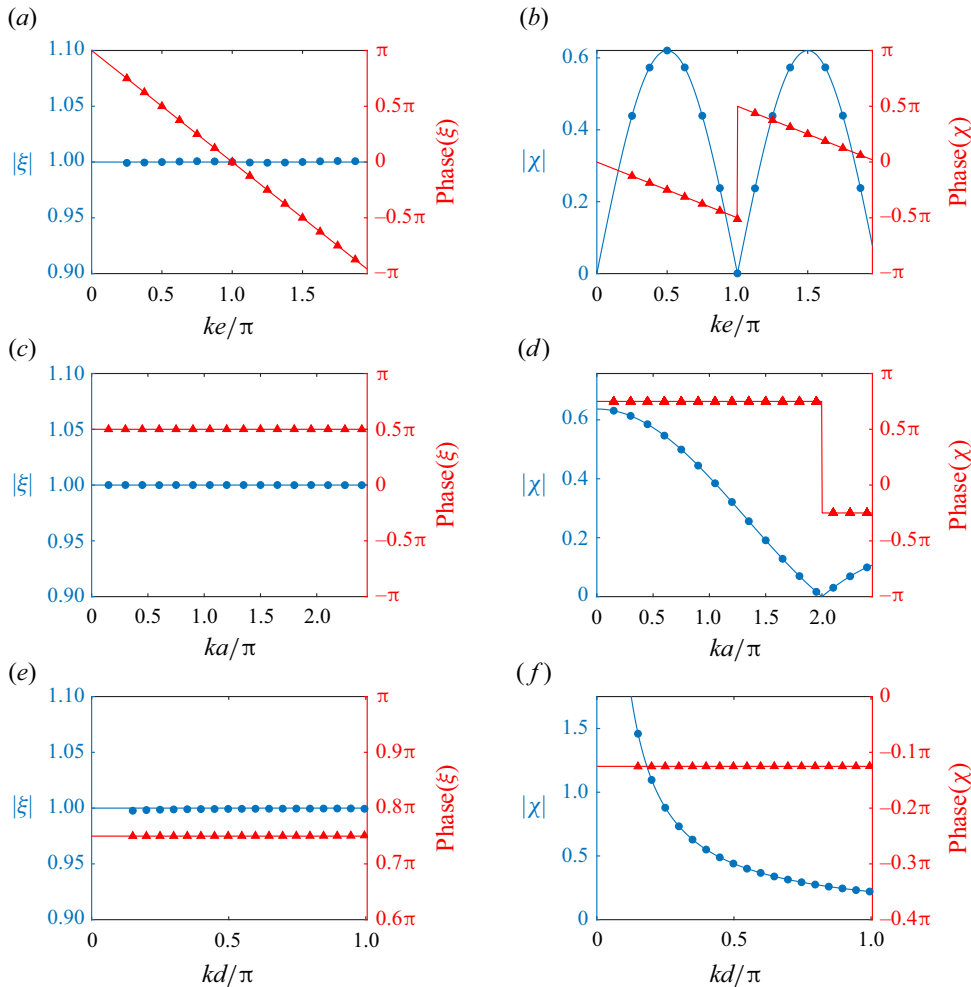
Figure 4. Numerical results – influence of the geometry on the conditions for perfect absorption. Source amplitude ratio $\xi = u_2/u_1$ (modulus and phase) and relative incident wave amplitude $\chi = \varphi_{inc}/(au_1)$ (modulus and phase) against the geometrical parameters: (*a,b*) the distance between the sources ke (fixing $kd = \pi/2$ and $ka = \pi/4$); (*c,d*) the source size ka ($kd = \pi/2$ and $ke = 2.5\pi$); and (*e,f*) the channel width kd ($ka = \pi/4$ and $ke = \pi/4$). The markers correspond to the numerical results, and the curves to the theoretical model.

3. Experimental realization of the active absorption

In our experiments, we use a channel with width $d = 50$ mm and length 1.2 m, maintaining a fixed water depth $h = 26$ mm. The dipole source is implemented by drilling two submerged openings on one of the vertical walls of the channel, each opening having width $a = 20$ mm and height $b = 10$ mm. The two openings are separated by a distance 5 mm (hence $e = 25$ mm) and placed at depth $h_o = 16$ mm (see figure 1). Each opening is connected to a cavity producing a controlled flux through its horizontal surface $S_p = 19 \times 19$ mm^2, with the flux created by the vertical motions of a rectangular piston with the same surface area, and controlled by a linear motor.

We measure the fields of the free surface elevation $\hat{\eta}(x, y, t)$ using an optical method known as Fourier transform profilometry (Cobelli *et al.* 2009; Maurel *et al.* 2009). This method relies on acquiring and analysing the fringe patterns projected onto the water

surface, with the water rendered diffusive by the addition of a dye (Przadka *et al.* 2012). Eventually, reflections at the free ends of the channel are minimized by using 5-degree sloping beaches. In scenarios without an incident wave in the channel ($\eta_{inc} = 0$), two beaches are positioned at the left and right ends of the channel. In the presence of an incident wave generated by a wavemaker at the left end of the channel, a single beach is used (at the right end of the channel).

3.1. *Active absorption in the harmonic regime*

In the harmonic regime, we proceed by controlling the two pistons independently at frequency ω and amplitudes p_1 and p_2. The conservation of fluxes implies that the mean velocities U_n, where $n = 1, 2$, satisfy $-\mathrm{i}\omega p_n S_p = ab U_n$. Consequently, from (2.8*a*,*b*) the velocities u_n used in the 2-D model are given approximatively by

$$u_n = -\mathrm{i}\alpha\omega \frac{S_p}{ab} p_n, \quad n = 1, 2, \tag{3.1}$$

with α defined in (2.8*a*,*b*). Next, the measured field of the free surface elevation $\hat{\eta}(x, y, t)$ provides $\eta(x, y)$ by Fourier transform, namely

$$\eta(x, y) = \frac{1}{T} \int_0^T \hat{\eta}(x, y, t)\, \mathrm{e}^{\mathrm{i}\omega t}\, \mathrm{d}t, \tag{3.2}$$

with T covering several periods (typically 20), and we now seek solutions in the far field of the form

$$\left.\begin{aligned} \eta(x, y) &\simeq \eta_{inc}\, \mathrm{e}^{\mathrm{i}kx} + \eta^-\, \mathrm{e}^{-\mathrm{i}kx}, && x \to -\infty, \\ \eta(x, y) &\simeq \eta^+\, \mathrm{e}^{\mathrm{i}kx}, && x \to +\infty, \end{aligned}\right\} \tag{3.3}$$

as in (2.9). With $\hat{\eta}(x, y, t) = -(1/g)\, \partial_t\phi(x, y, 0, t)$, and utilizing (2.3), (2.10) and (3.1), the complex amplitudes (η^-, η^+) can be written as

$$\left.\begin{aligned} \eta^- &= \mathrm{i}\beta \left(p_1\, \mathrm{e}^{-\mathrm{i}ke/2} + p_2\, \mathrm{e}^{\mathrm{i}ke/2}\right), \\ \eta^+ &= \eta_{inc} + \eta_0^+, \quad \eta_0^+ = \mathrm{i}\beta \left(p_1\, \mathrm{e}^{\mathrm{i}ke/2} + p_2\, \mathrm{e}^{-\mathrm{i}ke/2}\right), \end{aligned}\right\} \tag{3.4}$$

with β a non-dimensional parameter defined by

$$\beta = \frac{\omega^2}{g} \frac{S_p}{ab} \frac{\sin(ka/2)}{k^2 d} \alpha. \tag{3.5}$$

Accordingly, the conditions for perfect absorption read

$$p_1 = \frac{\eta_{inc}}{\chi_e}, \quad p_2 = \xi p_1, \tag{3.6a,b}$$

which is the equivalent of (2.13*a*,*b*), with $\xi = -\mathrm{e}^{-\mathrm{i}ke}$ and $\chi_e = 2\beta \sin(ke)\, \mathrm{e}^{-\mathrm{i}ke/2}$.

In our first experiments, we follow the same procedure as in our numerical simulations, using $\eta_{inc} = 0$, and measure the waves $\eta(x, y)$ generated by the dipole source in the harmonic regime. Following (2.13*a*,*b*), we aim to find the condition $p_2 = \xi p_1$ capable of experimentally producing $\eta^- = 0$ and characterize the corresponding values of $\chi_e = -\eta_0^+/p_1$. To achieve this, we set the frequency to $\omega = 14.5$ rad s^{-1}, corresponding to $kd \simeq \pi/2$, and conduct a series of 11×21 experiments with varying (p_1, p_2). The typical amplitude of each piston is $p_n \sim 5$ mm. Specifically, we consider 11 values of
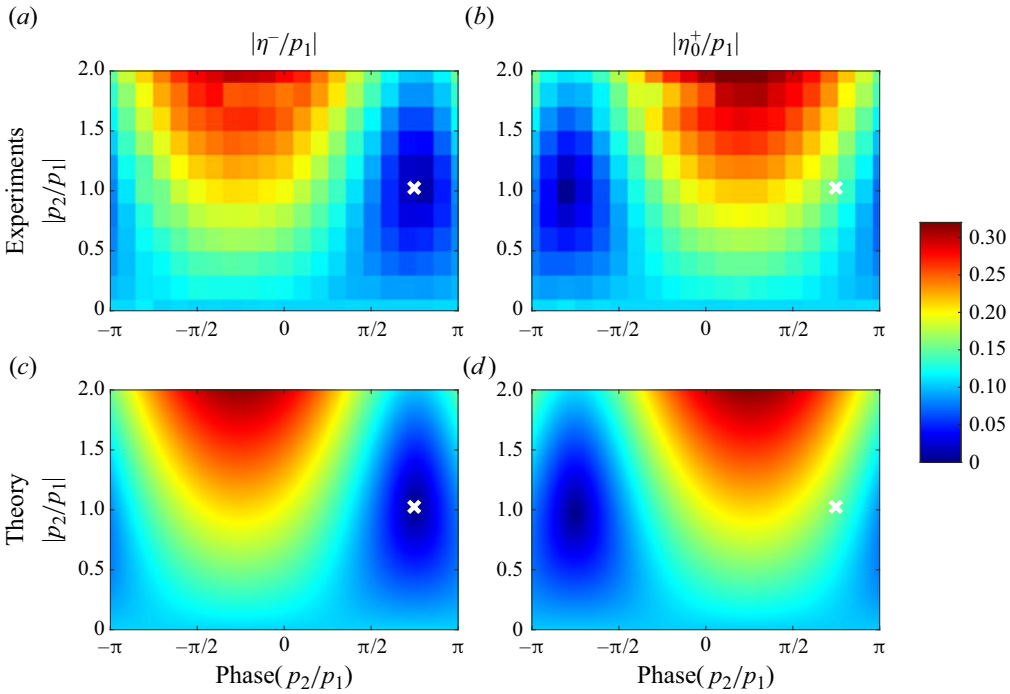
Figure 5. Amplitudes of the outgoing waves (η^-, η_0^+) normalized to p_1 as a function of the ratio p_2/p_1 (modulus and phase) obtained experimentally and theoretically (see (3.4)) for $\eta_{inc} = 0$. The white crosses indicate the theoretical prediction for $\eta^- = 0$. The frequency is $\omega = 14.5$ rad s^{-1} ($kd \simeq \pi/2$).

$|p_2/p_1| \in (0, 2)$, and for each modulus ratio, we vary the relative phase of (p_2/p_1) between $-\pi$ and π with a step of $\pi/20$. In each experiment, we measure the entire field $\eta(x, y)$, and by averaging it over y in the far field (sufficiently distant from the source), we determine the constant complex amplitudes (η^-, η_0^+). The results, depicted in figure 5, demonstrate good agreement with the theoretical model in (3.4). In particular, the agreement confirms (see white crosses in figure 5) that for $p_2/p_1 = \xi = -1.03\,\mathrm{e}^{-\mathrm{i}0.75} \simeq -\mathrm{e}^{-\mathrm{i}ke}$, the left-outgoing wave vanishes ($\eta^- \simeq 0$), and the corresponding value $\chi_e = -\eta_0^+/p_1 = 0.13\,\mathrm{e}^{-\mathrm{i}0.36}$ is consistent with (3.4).

In the next step, we quantitatively characterize the condition for perfect absorption across frequencies. Specifically, we vary the frequency within the range such that $k \in (0.2, 0.7)\pi/d$ and conduct a coarse version of the analysis depicted in figure 5, employing only 3×3 experiments centred on the theoretical value $p_2/p_1 = -\mathrm{e}^{-\mathrm{i}ke}$, resulting in $\eta^- = 0$. This is done by selecting $|p_2/p_1|$ from the set $\{0.9, 1, 1.1\}$, and the phase of (p_2/p_1) from $-ke + \pi\{0.96, 1, 1.04\}$; afterwards, linear interpolations are employed to determine the optimal condition for achieving perfect absorption. By repeating this experimental procedure four times, we obtained a refined mean prediction along with error bars derived from standard deviations. The conditions for perfect absorption are depicted in figure 6, illustrating $\xi = p_2/p_1$ (both modulus and phase), yielding $\eta^- = 0$, and the corresponding values of $\chi_e = \eta_{inc}/p_1 = -\eta_0^+/p_1$ across various frequencies. To compare with the model (3.6a,b) represented by solid lines in figure 6, ξ and χ_e were calculated using complex wavenumbers $k \to k + \mathrm{i}k_{im}$, where the small imaginary part $k_{im} = 2 \times 10^{-2}\,k^2 d$
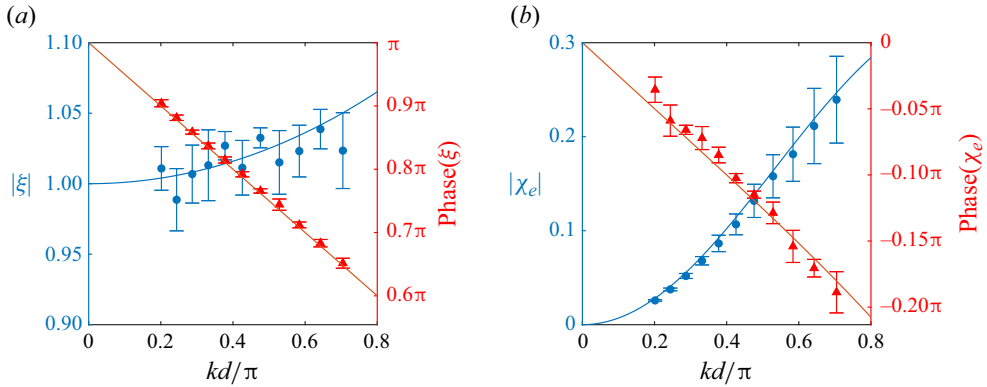
Figure 6. Experimental measurements – conditions for perfect absorption. Source amplitude ratio $\xi = p_2/p_1$ (modulus and phase) and relative incident wave amplitude $\chi_e = \eta_{inc}/p_1 = -\eta_0^+/p_1$ (modulus and phase) against the frequency by means of kd. The markers correspond to the experimental measurements, and the curves to the theoretical model (3.4), in which complex wavenumbers with a small imaginary part $k_{im} = 2 \times 10^{-2} k^2 d$ were used to account for attenuation, due to viscous losses.

accounts for attenuation due to viscous losses. This function fits the losses observed experimentally.

Eventually, figure 7 presents experimental evidence of perfect absorption when $\eta_{inc} \neq 0$. We generated η_{inc} at $\omega = 12.6$ rad s^{-1} ($kd = 0.42\pi$) using a plunging-type wavemaker placed at the left end of the waveguide and controlled by a linear motor. The complex amplitude η_{inc} was characterized in a preliminary study (not reported), in the absence of dipolar source ($p_1 = p_2 = 0$). This allowed us to determine the complex amplitudes (p_1, p_2) producing perfect absorption, according to (3.6a,b), which was validated in figure 6. In practice, generating the incident waves and those emitted by the dipole source is achieved by synchronizing the three linear motors. Figure 7(a) displays the corresponding $\eta(x, y)$ (real part) derived from the measured field $\hat{\eta}(x, y, t)$ using (3.2). For comparison, figure 7(b) presents the result obtained via numerical computation in two dimensions under the same conditions. The profile of η along x reported in figure 7(c) represents an average of $\eta(x, y)$ over y. It reveals weak outgoing waves, with η^+ approaching zero for $x \gtrsim 2a$, and η without the characteristic beatings indicative of the superposition of left- and right-going waves for $x \lesssim -2a$, hence $\eta^- \sim 0$. To further quantify the smallness of η^- and η^+, fits of η were conducted for x in the ranges $(-0.4, -0.05)$ cm and $(0.05, 0.4)$ cm, utilizing $k_{im} = 2 \times 10^{-2} k^2 d$ as done previously. This procedure was repeated for 11 frequencies corresponding to kd in the range $(0.2, 0.7)\pi$. The results of this series of experiments are presented in figure 7(d), confirming consistent absorption efficiency with $(|\eta^-/\eta_{inc}|^2 + |\eta^+/\eta_{inc}|^2)$ at approximately 10^{-3} over the entire frequency range, signifying 99.9 % absorption.

3.2. *Active absorption in the transient regime*

To conclude our experimental demonstration of perfect absorption, we investigate an incoming wave signal in the transient regime. This signal is generated based on its Fourier transform $\eta_{inc}(\omega)$, randomly distributed in phase and modulus but constrained
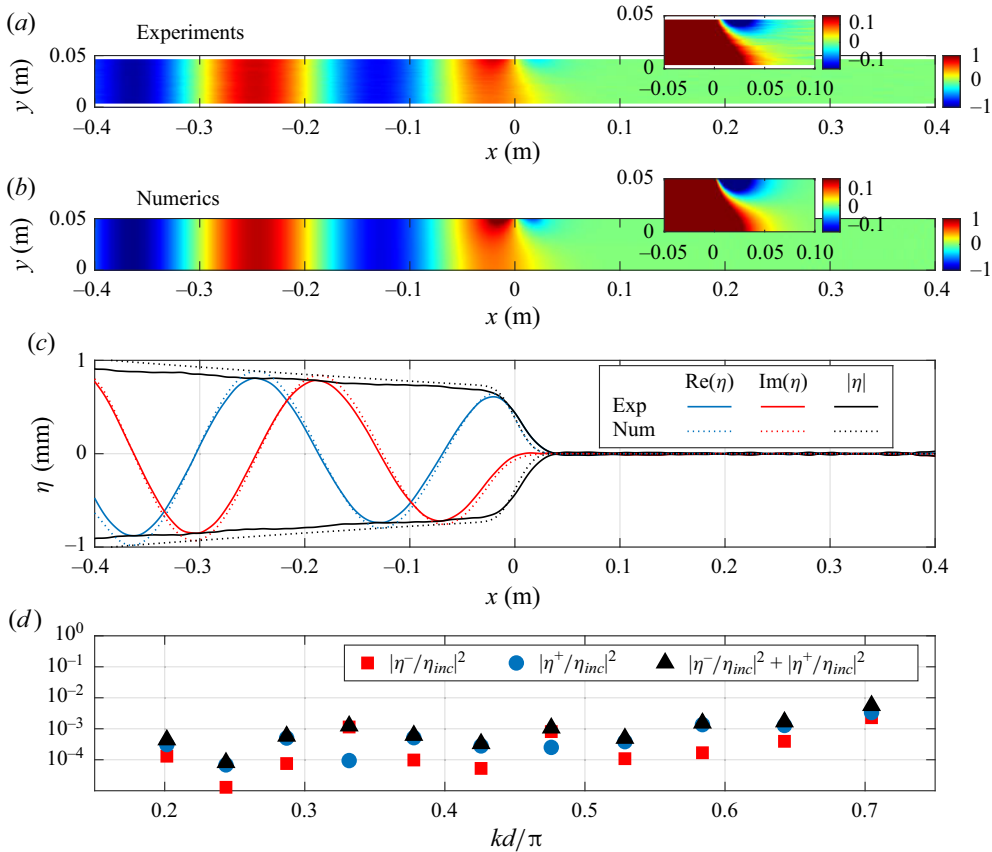
Figure 7. (*a*) Real part of $\eta(x, y)$ measured experimentally, for $\omega = 12.6$ rad s^{-1} (corresponding to an incident wavenumber $kd/\pi = 0.42$). (*b*) Same results from direct numerics. (*c*) Average in y of $\eta(x, y)$. (*d*) Left-going and right-going energies, normalized to the incident one, against the incident wavenumber kd/π.

by a Gaussian profile, specifically

$$
\left.
\begin{aligned}
&\eta_{inc}(\omega) \text{ random with } |\eta_{inc}(\omega)| < \eta_0 \exp\left(-\frac{(\omega - \omega_0)^2}{\sigma^2}\right), \\
&\hat{\eta}_{inc}(x, t) = \int_0^\infty \eta_{inc}(\omega) \exp(\mathrm{i}(kx - \omega t))\, \mathrm{d}\omega,
\end{aligned}
\right\}
\tag{3.7}
$$

with parameters $\eta_0 = 0.08$ mm, $\omega_0 = 14.5$ rad s^{-1} and $\sigma = 4$ rads^{-1} (see figure 8*e*). In practice, we consider $N = 100$ discrete frequencies $\omega_i \in (1, 30)$ rad s^{-1}. Leveraging our earlier study in the harmonic regime, where we identified $\eta_{inc}(\omega)/p_1(\omega)$ and $p_2(\omega)/p_1(\omega)$ for perfect absorption (figure 6 and (3.6*a,b*)), we generate $\hat{p}_1(t)$ and $\hat{p}_2(t)$ through Fourier transforms.

The primary result is presented in figure 8(*a*), which illustrates a space–time diagram of the signal $\hat{\eta}(x, t)$ averaged over $y \in (0, d)$. The effective absorption attributable to the dipole source centred at $x = 0$ is evident. Indeed, $\hat{\eta}(x, t)$ remains constant in shape over time for any $x \lesssim -2a$ up to slight attenuation during propagation, while it is nearly zero for $x \gtrsim 2a$. These characteristic shapes are illustrated for $x = -0.2$ m and $x = 0.2$ m in figure 8(*b*). To evaluate absorption quantitatively, we analyse the amplitudes in Fourier
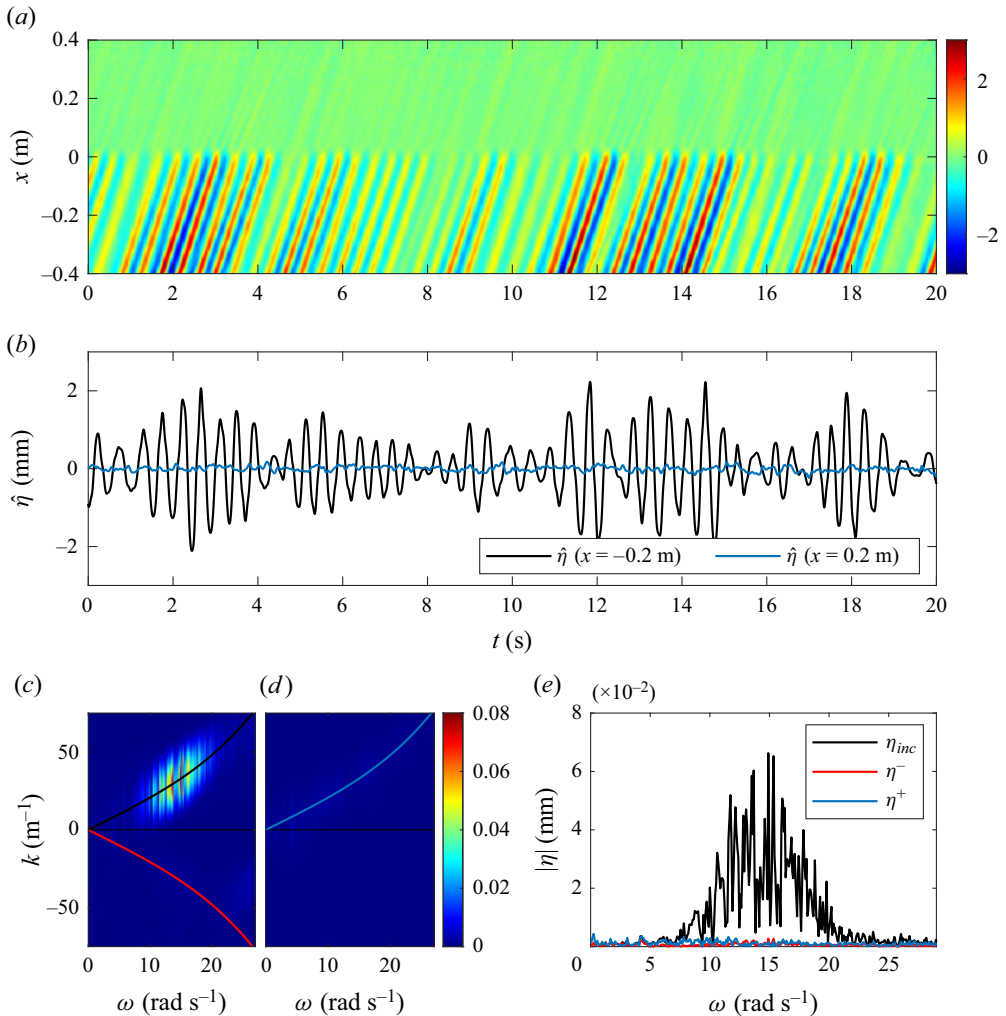
990 A9-11

Figure 8. (*a*) Space–time diagram $\eta(x, t)$, average in y of $\eta(x, y, t)$, reporting the propagation of an incident wave generated following (3.6*a,b*) and its interaction with the dipole source tuned to achieve perfect absorption. (*b*) Time signal before (at $x = -0.2$ m) and after (at $x = 0.2$ m) the dipolar source. (*c,d*) Space and time Fourier transforms $|\hat{\eta}(k, \omega)|$ calculated for $x < 0$ and $x > 0$, revealing vanishing outgoing waves, all the energy corresponding to the incident wave η_{inc} in alignment with the theoretical dispersion (black line in *c*). (*e*) Wave amplitude along the dispersion relation of the incident and outgoing waves.

space $\eta(k, \omega)$ in these two regions utilizing

$$\eta^{\pm}(k, \omega) = \int_{x_1^{\pm}}^{x_2^{\pm}} \int_0^T \hat{\eta}(x, t) \exp(\mathrm{i}(\omega t - kx)) \, \mathrm{d}x \, \mathrm{d}t, \tag{3.8}$$

with $T = 20$ s, $(x_1^-, x_2^-) = (-0.4 \text{ m}, 0)$ and $(x_1^+, x_2^+) = (0, 0.4 \text{ m})$ (before and after the dipole). Results in the (k, ω) plane are shown in figures 8(*c*) and 8(*d*), respectively. In figure 8(*c*), it is notable that the spectral content of $\eta^-(k, \omega)$ is almost zero for $k < 0$, particularly along the dispersion line $k = -k(\omega)$ (solid red line), and lies predominantly along the dispersion line $k = k(\omega) > 0$ (solid black line), hence associated with the right-going wave only. This confirms $\eta^- = 0$. Similarly, figure 8(*d*) demonstrates that the

990 A9-12

spectral content of $\eta^+(k, \omega)$ along the line $k = k(\omega)$ is nearly zero. The amplitude along each dispersion line is shown in figure 8(*e*). These observations are further quantified by deriving a measure of the energy of the incident, left-going and right-going waves by calculating the energies along these lines, namely

$$
\left.
\begin{aligned}
E_{inc} = \int_0^{2\omega_0} |\eta^-(+k(\omega), \omega)|^2 \, \mathrm{d}\omega, \quad E^- = \int_0^{2\omega_0} |\eta^-(-k(\omega), \omega)|^2 \, \mathrm{d}\omega, \\
E^+ = \int_0^{2\omega_0} |\eta^+(+k(\omega), \omega)|^2 \, \mathrm{d}\omega,
\end{aligned}
\right\}
\tag{3.9}
$$

resulting in an absorption $(E_{inc} - E^- - E^+)/E_{inc} = 99.5\,\%$.

4. Concluding remarks

The active absorption device that we have proposed is inspired by two absorption systems. First, it takes up the concept of conventional active absorption, which traditionally works only in reflection, and is extended here to encompass both reflection and transmission, independently of viscous losses. Second, it is inspired by a passive device for which we had demonstrated a relationship between the amplitudes of the resonators and that of the incident wave leading to perfect absorption (Euvé *et al.* 2023). We have adopted this relationship in the active system, thus avoiding dependence on the level of loss and extending its range of frequency validity. This has been demonstrated for waves guided in a channel. It should be noted, however, that following the developments proposed for active absorbers in reflection in Schäffer & Klopman (2000), our absorber should be applicable to unguided configurations and arbitrary incidences.

Declaration of interests. The authors report no conflict of interest.

Author ORCIDs.
Léo-Paul Euvé https://orcid.org/0009-0006-7757-643X;
Kim Pham https://orcid.org/0000-0001-8767-6457;
Philippe Petitjeans https://orcid.org/0000-0003-3179-0108;
Vincent Pagneux https://orcid.org/0000-0003-2019-823X;
Agnès Maurel https://orcid.org/0000-0001-8432-9871.

Appendix A. Additional information on the derivation of (φ^-, φ^+)

We define $\psi(x, y)$ as a test function satisfying

$$
\left.
\begin{aligned}
\Delta \psi + k^2 \psi = 0, \quad \text{in } \Sigma, \\
\frac{\partial \psi}{\partial y}\bigg|_\gamma = \frac{\partial \psi}{\partial y}\bigg|_{\gamma_i} = 0, \quad i = 1, 2.
\end{aligned}
\right\}
\tag{A1}
$$

The derivation of the Green's identity proceeds as follows. First, we define the finite 2-D domain $\Sigma_m = \{x \in (-x_m, x_m), y \in (0, d)\}$ with $x_m > (e + a)/2$. Then we subtract the product of the first equation in (2.6) with ψ from the product of the first equation of (A1)

with φ, integrating over Σ_m. Employing integration by parts yields

$$\int_{\partial \Sigma_m} \left(\psi \, \frac{\partial \varphi}{\partial n} - \varphi \, \frac{\partial \psi}{\partial n} \right) \mathrm{d}s = 0, \tag{A2}$$

where $\partial \Sigma_m = \{x \in (-x_m, x_m), y \in \{0, d\}\} \cup \gamma^+ \cup \gamma^-$ with $\gamma^\pm = \{x = \pm x_m, y \in (0, d)\}$. Further, taking into account the boundary conditions on γ_i, $i = 1, 2$ (along with Neumann conditions on the rigid walls), we obtain

$$-\int_{\gamma^-} \left(\psi \, \frac{\partial \varphi}{\partial x} - \varphi \, \frac{\partial \psi}{\partial x} \right) \mathrm{d}y + \int_{\gamma^+} \left(\psi \, \frac{\partial \varphi}{\partial x} - \varphi \, \frac{\partial \psi}{\partial x} \right) \mathrm{d}y$$
$$+ u_1 \int_{\gamma_1} \psi(x, d) \, \mathrm{d}x + u_2 \int_{\gamma_2} \psi(x, d) \, \mathrm{d}x = 0. \tag{A3}$$

Subsequently, setting $\psi(x, y) = \mathrm{e}^{-\mathrm{i}kx}$ and taking into account that ψ is orthogonal to the evanescent field on γ^+ and γ^-, along with the far-field solution for φ in (2.9), we obtain

$$2\mathrm{i}kd(-\varphi_{inc} + \varphi^+) + 2 \, \frac{\sin ka/2}{k} \left(u_1 \, \mathrm{e}^{\mathrm{i}ke/2} + u_2 \, \mathrm{e}^{-\mathrm{i}ke/2} \right) = 0, \tag{A4}$$

leading to the second relation in (2.10). Analogously, repeating the calculation with $\psi(x, y) = \mathrm{e}^{\mathrm{i}kx}$ yields the first relation in (2.10).

Appendix B. The cases of inactive sources: existence of localized eigenmodes

Here, we revisit the concept of what we previously termed 'inactive sources', which, from (2.10), yield $\varphi^- = \varphi_0^+ = 0$ regardless of the value of φ_{inc}. First, we define the problem set for φ_1 that satisfies the Helmholtz equation with $\partial_y \varphi_1 = u_1$ on γ_1, and Neumann boundary conditions on γ and γ_2. We seek solutions to this problem that decay exponentially to 0 when $x \to \pm\infty$. Through integration of the Helmholtz equation over the domain Σ, and application of the divergence theorem, we obtain

$$u_1 = -\frac{k^2}{a} \int_\Sigma \varphi_1(x, y) \, \mathrm{d}x \, \mathrm{d}y. \tag{B1}$$

Consequently, we can formulate the eigenvalue problem

$$\left. \begin{array}{l} (\Delta + k^2)\varphi_1 = 0, \quad \text{in } \Sigma, \\[2mm] \dfrac{\partial \varphi_1}{\partial y}\bigg|_{\gamma \cup \gamma_2} = 0, \quad \dfrac{\partial \varphi_1}{\partial y}\bigg|_{\gamma_1} = -\dfrac{k^2}{a} \displaystyle\int_\Sigma \varphi_1(x, y) \, \mathrm{d}x \, \mathrm{d}y, \end{array} \right\} \tag{B2}$$

whose eigenvalues belong to the set $ka = 2n\pi$, where n is an integer satisfying $n < d/(2a)$, to satisfy $kd < \pi$ (this condition ensures the presence of a single propagating mode in the guide).

Next, we expand our investigation to include problem (2.6) with the condition that φ decreases exponentially to 0 when $x \to \pm\infty$. By integrating the Helmholtz equation over Σ, and considering the boundary condition over γ, γ_1 and γ_2, along with the condition
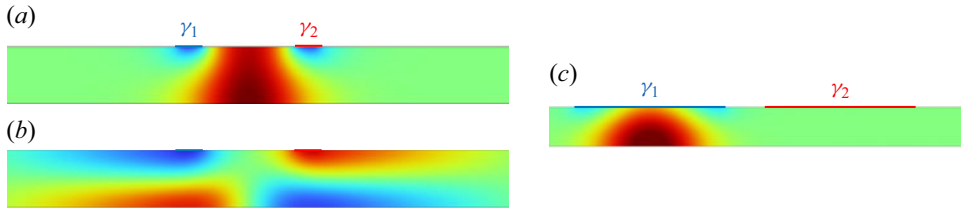
Figure 9. (*a*,*b*) Eigenmodes for $e/d = 2$ and $a/d = 0.5$ associated with the first two eigenvalues k^2 of (B5) found numerically at $(kd)^2 = 2.47$ and 9.86, hence $ke = \pi$ and 2π. (*c*) Eigenmode for $e/d = 5$ and $a/d = 4$ associated with the first eigenvalue k^2 of (B2) found numerically at $(kd)^2 = 2.47$, hence $ka = 2\pi$.

when $x \to \pm\infty$, we obtain

$$u_1 + u_2 = -\frac{k^2}{a} \int_\Sigma \varphi(x, y) \, \mathrm{d}x \, \mathrm{d}y. \tag{B3}$$

Furthermore, by multiplying the Helmholtz equation by x and integrating over Σ, we obtain

$$-u_1 + u_2 = -\frac{2k^2}{ea} \int_\Sigma x \, \varphi(x, y) \, \mathrm{d}x \, \mathrm{d}y. \tag{B4}$$

By combining (B3) and (B4), we formulate an eigenvalue problem defined by

$$\left. \begin{aligned} (\Delta + k^2) \, \varphi(x, y), \quad &\text{in } \Sigma, \\ \frac{\partial \varphi}{\partial y}_{|\gamma} &= 0, \\ \frac{\partial \varphi}{\partial y}_{|\gamma_1} &= -\frac{k^2}{2a} \int_\Sigma \varphi(x, y) \left(1 - \frac{2x}{e} \right) \mathrm{d}x \, \mathrm{d}y, \\ \frac{\partial \varphi}{\partial y}_{|\gamma_2} &= -\frac{k^2}{2a} \int_\Sigma \varphi(x, y) \left(1 + \frac{2x}{e} \right) \mathrm{d}x \, \mathrm{d}y, \end{aligned} \right\} \tag{B5}$$

with φ decreasing exponentially to 0 when $x \to \pm\infty$. Solving (B5) yields eigenvalues $ke = n\pi$ (while ensuring $kd < \pi$), with symmetric eigenmodes when n is odd (and $u_1 - u_2 = 0$ from (B4)), and antisymmetric eigenmodes when n is even (and $u_1 + u_2 = 0$ from (B3)). Additionally, it provides eigenvalues for $ka = 2n\pi$, associated with eigenmodes that are the superposition of an eigenmode φ_1 solution of (B2) and its counterpart φ_2 when the roles of γ_1 and γ_2 are exchanged.

Figures 9(*a*,*b*) depict typical eigenmodes calculated (using Comsol) by solving the eigenvalue problem (B5) in the geometry corresponding to the results in figures 4(*a*,*b*), wherein the first two eigenvalues are obtained numerically for $ke \simeq \pi$ and 2π. Additionally, figure 9(*c*) presents the first eigenmode for $ka \simeq 2\pi$ in the geometry corresponding to the results in figures 4(*c*,*d*). In these scenarios, perfect absorptions ($\varphi^- = \varphi_0^+ = 0$) were achieved for $\varphi_{inc} = 0$, as the boundary conditions imposed by the sources coincide with those satisfied by an eigenmode.

REFERENCES

BARMAN, K.K. & BORA, S.N. 2021 Linear water wave interaction with a composite porous structure in a two-layer fluid flowing over a step-like sea-bed. *Geophys. Astrophys. Fluid Dyn.* **115** (5–6), 577–611.

VAN DEN BREKEL, E. 2021 Hydrodynamic and ecological performance of a new modular unit for living breakwaters: wave flume experiments and results. PhD thesis, TU Delft Civil Engineering and Geosciences.

COBELLI, P.J., MAUREL, A., PAGNEUX, V. & PETITJEANS, P. 2009 Global measurement of water waves by Fourier transform profilometry. *Exp. Fluids* **46** (6), 1037–1047.

EUVÉ, L.-P., PHAM, K., PORTER, R., PETITJEANS, P., PAGNEUX, V. & MAUREL, A. 2023 Perfect resonant absorption of guided water waves by Autler–Townes splitting. *Phys. Rev. Lett.* **131** (20), 204002.

VAN GENT, M., BUIS, L., VAN DEN BOS, J.P. & WÜTHRICH, D. 2023 Wave transmission at submerged coastal structures and artificial reefs. *Coast. Engng* **184**, 104344.

GUO, B. & RINGWOOD, J.V. 2021 A review of wave energy technology from a research and commercial perspective. *IET Renew. Power Gen.* **15** (14), 3065–3090.

JIN, S. & GREAVES, D. 2021 Wave energy in the UK: status review and future perspectives. *Renew. Sust. Energ. Rev.* **143**, 110932.

MAUREL, A., COBELLI, P., PAGNEUX, V. & PETITJEANS, P. 2009 Experimental and theoretical inspection of the phase-to-height relation in Fourier transform profilometry. *Appl. Opt.* **48** (2), 380–392.

VAN DER MEER, J.W., BRIGANTI, R., ZANUTTIGH, B. & WANG, B. 2005 Wave transmission and reflection at low-crested structures: design formulae, oblique wave attack and spectral change. *Coast. Engng* **52** (10–11), 915–929.

MILGRAM, J.H. 1965 Compliant water wave absorbers. PhD thesis, Massachusetts Institute of Technology.

MILGRAM, J.H. 1970 Active water-wave absorbers. *J. Fluid Mech.* **42** (4), 845–859.

PRZADKA, A., CABANE, B., PAGNEUX, V., MAUREL, A. & PETITJEANS, P. 2012 Fourier transform profilometry for water waves: how to achieve clean water attenuation with diffusive reflection at the water surface? *Exp. Fluids* **52**, 519–527.

SALTER, S.H. 1974 Wave power. *Nature* **249** (5459), 720–724.

SCHÄFFER, H.A. & KLOPMAN, G. 2000 Review of multidirectional active wave absorption methods. *ASCE J. Waterway Port Coastal Ocean Engng* **126** (2), 88–97.

SILVA, R., SALLES, P. & PALACIO, A. 2002 Linear waves propagating over a rapidly varying finite porous bed. *Coast. Engng* **44** (3), 239–260.

SOLLITT, C.K. & CROSS, R.H. 1972 Wave transmission through permeable breakwaters. In *Coastal Engineering 1972*, pp. 1827–1846. ASCE.

ZHU, S. 2001 Water waves within a porous medium on an undulating bed. *Coast. Engng* **42** (1), 87–101.